

Dendritic Domain-Specific Sampling of Long-Range Axons Shapes Feedforward and Feedback Connectivity of L5 Neurons

Alessandro R. Galloni,^{1,2} Zhiwen Ye,¹ and  Ede Rancz¹

¹The Francis Crick Institute, London NW1 1AT, United Kingdom, and ²University College London, London WC1E 6BT, United Kingdom

Feedforward and feedback pathways interact in specific dendritic domains to enable cognitive functions such as predictive processing and learning. Based on axonal projections, hierarchically lower areas are thought to form synapses primarily on dendrites in middle cortical layers, whereas higher-order areas are thought to target dendrites in layer 1 and in deep layers. However, the extent to which functional synapses form in regions of axodendritic overlap has not been extensively studied. Here, we use viral tracing in the secondary visual cortex of male mice to map brain-wide inputs to thick-tufted layer 5 pyramidal neurons. Furthermore, we provide a comprehensive map of input locations through subcellular optogenetic circuit mapping. We show that input pathways target distinct dendritic domains with far greater specificity than appears from their axonal branching, often deviating substantially from the canonical patterns. Common assumptions regarding the dendrite-level interaction of feedforward and feedback inputs may thus need revisiting.

Key words: connectivity; dendrites; feedback; rabies; sCRACM; visual cortex

Significance Statement

Perception and learning depend on the ability of the brain to shape neuronal representations across all processing stages. Long-range connections across different hierarchical levels enable diverse sources of contextual information, such as predictions or motivational state, to modify feedforward signals. Assumptions regarding the organization of this hierarchical connectivity have not been extensively verified. Here, we assess the synaptic connectivity of brain-wide projections onto pyramidal neurons in the visual cortex of mice. Using trans-synaptic viral tracing and subcellular optogenetic circuit mapping, we show that functional synapses do not follow the consistent connectivity rule predicted by their axonal branching patterns. These findings highlight the diversity of computational strategies operating throughout cortical networks and may aid in building better artificial networks.

Introduction

Hierarchical connectivity between cortical areas is often considered a central organizing principle underlying computations in the brain (Harris et al., 2019; Vezoli et al., 2021). An important aspect of this hierarchy is the interaction between feedforward (FF) and feedback (FB) signals, allowing neurons closer to the

sensory input to adapt their responses based on high-level knowledge and objectives. How FF and FB signals are combined within individual neurons is an important unresolved problem with implications for our understanding of computation in both biological and artificial networks (Larkum, 2013; Guerguiev et al., 2017; Aru et al., 2020).

In areas close to the sensory periphery, like the primary visual cortex (VISp), inputs can easily be designated as FF and FB. However, the recurrent nature of intracortical and thalamocortical connectivity makes it more difficult to unambiguously categorize inputs in secondary sensory and associative areas. How then are FF and FB projections defined? Axonal pathways to visual cortical areas have distinctive laminar projection patterns that are broadly aligned with the hierarchy inferred from visual responses of neurons in each region. Specifically, FF projections mostly terminate in middle layers, particularly layer 4 (L4), whereas FB projections primarily target L1, and to a lesser extent, deeper layers (Rockland and Pandya, 1979). Similar projection patterns also appear in many other higher level areas and have

Received Aug. 10, 2021; revised Dec. 30, 2021; accepted Jan. 5, 2022.

Author contributions: A.R.G. and E.R. designed research; A.R.G. and Z.Y. performed research; A.R.G., Z.Y., and E.R. analyzed data; A.R.G. and E.R. wrote the paper.

This work was supported by the Wellcome Trust (104285/B/14/Z) and the Francis Crick Institute, which receives its core funding from Cancer Research UK (FC001153), the United Kingdom Medical Research Council (FC001153), and the Wellcome Trust (FC001153), and a Boehringer Ingelheim Fonds PhD Fellowship to A.R.G. We thank Troy Margrie and Molly Strom for viral constructs, Rob Campbell and Charlie Rousseau for help with data acquisition and analysis of rabies tracing experiments, Joe Brock for help with illustrations, and Florencia Iacuruso and Zoltán Kisvárdy for comments on the manuscript.

The authors declare no competing financial interests.

Correspondence should be addressed to Ede Rancz at ede.rancz@crick.ac.uk.

<https://doi.org/10.1523/JNEUROSCI.1620-21.2022>

Copyright © 2022 the authors

thus been used as a proxy to describe their hierarchical relationships (Felleman and Van Essen, 1991; Harris et al., 2019; D'Souza et al., 2020; Wang et al., 2020b).

At the single-cell level, these projection patterns imply that FF and FB projections may converge on different dendritic domains in individual neurons whose dendrites span multiple layers. Thick-tufted layer 5 (ttL5) neurons in particular have large dendritic trees spanning all cortical layers and biophysical properties that support highly nonlinear integration of inputs and are thus at the center of many theories of hierarchical computation in the brain (Larkum, 2013; Guerguiev et al., 2017; Payeur et al., 2021). A common feature in these theories is FF connections targeting basal dendrites and FB connections synapsing onto the apical tuft in L1. This is based on the assumption that synapses form in the regions of greatest overlap between axons and dendrites, a principle known as Peters' rule (Rees et al., 2017). Projections, however, do not guarantee functional connections. Although at the level of local interneuron connectivity there is some support for Peters' rule (Fino and Yuste, 2011; Packer et al., 2013; Rieubland et al., 2014), its general applicability has been refuted by dense anatomic reconstructions of retinal (Briggman et al., 2011; Helmstaedter et al., 2013; Kim et al., 2014; Krishnaswamy et al., 2015) and local excitatory cortical circuits (Kasthuri et al., 2015; Lee et al., 2016). Poor prediction of dendritic input by axonal distribution has been shown for some long-range connections (Petreanu et al., 2009; Little and Carter, 2012), but little is known about the general adherence to Peters' rule at the level of long-range connectivity as it hasn't been systematically studied.

To investigate how Peters' rule applies to long-range projections, subcellular channelrhodopsin-assisted circuit mapping (sCRACM; Petreanu et al., 2009) can be used. By selectively stimulating axons from specific input areas at different locations, highly specific dendritic targeting can be revealed (Yamawaki et al., 2019; Anastasiades et al., 2021). Here, we used a combination of monosynaptically restricted rabies tracing (Kim et al., 2015; Reardon et al., 2016) and sCRACM recordings to comprehensively describe the functional input connectivity to ttL5 pyramidal neurons in medial secondary visual cortex and test whether Peters' rule is valid for this neural population. We find that canonical FF and FB projection profiles do not match functional subcellular input maps, and thus hierarchical connectivity motifs should not be assumed based on axon and dendrite distributions alone.

Materials and Methods

Animals. All animal experiments were prospectively approved by the local ethics panel of the Francis Crick Institute (previously National Institute for Medical Research) and the United Kingdom Home Office under the Animals (Scientific Procedures) Act 1986 (PPL 70/8935). *Tg(Colgal2-Cre)NF107Gsat* (catalog #036504-UCD, MMRRC; RRID: MMRRC_036504-UCD) mice crossed with the Ai14 reporter line expressing tdTomato (catalog #JAX:007908, The Jackson Laboratory; RRID:IMSR_JAX:007908) were used throughout this work. *Tg(Rbp4-Cre)KL100Gsat/Mmucd* (catalog #031125-UCD, MMRRC; RRID: MMRRC_031125-UCD) mice were used to establish the efficacy of the Cre-off approach. As only male mice are transgenic in the *Colgal2-Cre* line, all experiments were done on male animals.

Viruses. EnvA-CVS-N2c^{AG}-mCherry rabies virus, and adeno-associated viruses (AAVs) expressing TVA and EGFP (AAV8-EF1a-flex-GT), N2c glycoprotein (AAV1-Syn-flex-H2B-N2CG), or Cre-OFF Chronos-GFP (AAV1-EF1-CreOff-Chronos-GFP) were a gift from Molly Strom and Troy Margrie. Chronos-GFP (also called ShChR) expressing adeno-associated virus (rAAV1-Syn-Chronos-GFP) was obtained from the Vector Core at the University of North Carolina at Chapel Hill.

Table 1. Stereotaxic coordinates for viral injections

Area	AP	ML	DV	No. injections
VISp	[−3.5, −2.8]	[1.8, 2.7]	[0.5, 0.6]	3
V2M	[−3.2, −2.7]	1	[0.2, 0.4]	2
RSPg	[−3.2, −2.7]	[0.4, 0.5]	[0.5, 0.7]	2
ACA	[0, 1.1]	[0.4, 0.5]	[1.2, 1.5]	3
ORB	[+2, +2.8]	1	[1.5, 2.3]	3
ATN	[−1.1, −0.5]	[0.5, 0.7]	[3.2, 3.3]	2
LP	[−2.3, −1.7]	[1.4, 1.5]	[2.4, 2.6]	3

Distances in mm, AP from bregma, DV from pia. Square brackets denote a range [minimum, maximum].

Surgical procedures. Surgeries were performed on mice aged 3–8 weeks using aseptic technique under isoflurane (2–4%) anesthesia and analgesia (meloxicam 2 mg/kg and buprenorphine 0.1 mg/kg). The animals were head fixed in a stereotaxic frame, and a small hole (0.5–0.7 mm) was drilled in the skull above the injection site. Viruses were injected using a Nanoject III delivery system (Drummond Scientific) at 0.4 nl/s.

For rabies virus tracing experiments, a 1:2 mixture of TVA and N2c glycoprotein expressing Cre-dependent AAVs (10–20 nl) was injected [anteroposterior (AP), lambda point −0.8 mm; mediolateral (ML), 1.6 mm; dorsoventral (DV), 0.6 mm]. Rabies virus (50–100 nl) was injected 5–7 d later. Ten to 12 d later, animals were transcardially perfused under terminal anesthesia with cold phosphate buffer (PB, 0.1 M) followed by 4% paraformaldehyde (PFA) in PB (0.1 M).

For the sCRACM experiments, Chronos-GFP-expressing AAV was injected into one of the identified presynaptic regions. The range of stereotaxic coordinates, targeted to the location of the densest rabies labeling in each input region, are listed in Table 1. In the medial secondary visual cortex (V2M), Cre-OFF Chronos-GFP was instead used to avoid expression in the recorded Colgal2-Cre neurons. For injections into lateral posterior nucleus (LP), the Chronos-GFP virus was diluted by 10-fold in sterile cortex buffer before injection to eliminate retrograde labeling of V2M neurons.

Data acquisition and analysis for rabies tracing experiments. Brain samples were embedded in 4–5% agarose (catalog #90123-6-6, Sigma-Aldrich) in 0.1 M PB and imaged using serial two-photon tomography (Ragan et al., 2012; Osten and Margrie, 2013; Han et al., 2018). Eight optical sections were imaged every 5 μ m with 1.2 μ m \times 1.2 μ m lateral resolution, after which a 40 μ m physical section was removed. Excitation was provided by a pulsed femtosecond laser at 800 nm wavelength (Mai Tai eHP, Spectra-Physics). Images were acquired through a 16 \times /0.8 NA objective (catalog #MRP07220, Nikon) in three channels (green, red, blue) using photomultiplier tubes. Image tiles for each channel and optical plane were stitched together using custom-written MATLAB scripts (<https://github.com/SainsburyWellcomeCentre/StitchIt>). For cell detection, full resolution images were first filtered with a Gaussian blur (sigma = 1) using Fiji (ImageJ 1.52e) to reduce imaging noise. The open-source package cellfinder (Tyson et al., 2021) was used for cell candidate detection and classification. Automated mouse atlas propagation (Niedworok et al., 2016) was used for registration and segmentation [Allen Common Coordinate Framework (Allen CCFv3); Wang et al., 2020a]. For cell density visualization, cell coordinates were reverse transformed onto the Allen CCFv3 space using Elastix (Klein et al., 2010).

Acute slice preparation and electrophysiological recordings. Adult mice were anesthetized with isoflurane and decapitated at least 17 d after the viral injection. The brain was rapidly removed and placed in oxygenated ice-cold slicing solution containing the following (in mM): 125 sucrose, 62.5 NaCl, 2.5 KCl, 1.25 NaH₂PO₄, 26 NaHCO₃, 1 CaCl₂, 25 dextrose; osmolarity 340–350 mOsm. Coronal slices (300 μ m) containing V2M were prepared using a vibrating blade microtome (Leica VT1200S). Slices were kept submerged in artificial (A)CSF, containing the following (in mM): 125 NaCl, 2.5 KCl, 1.25 NaH₂PO₄, 26 NaHCO₃, 1 MgCl₂, 2 CaCl₂, 25 dextrose; osmolarity 308–312 mOsm) at 35°C for the first 30–60 min after slicing, then at room temperature (22°C). All solutions were continuously bubbled with carbogen (95% O₂/5% CO₂).

The recording chamber was perfused at a rate of 6 ml/min with ACSF at room temperature (22°C). To prevent axonal spike propagation and enhance responses to optical stimulation, 1 μ M tetrodotoxin (TTX) and 100 μ M 4-aminopyridin (4-AP) were added to the recording ACSF. Filamented borosilicate glass micropipettes were pulled and heat polished using a horizontal puller (Zeitz DMZ Universal Electrode Puller) to obtain an electrode resistance of 3–6 M Ω . The glass electrodes were filled with an internal solution containing the following (in mM): 120 CsMeSO₃ (CH₃O₃SCs), three CsCl, 10 HEPES, 1 EGTA, 4 Na₂ATP, 0.3 NaGTP, 5 Na₂-phosphocreatine (C₄H₈N₃O₅PN₂), 3.5 QX-314 chloride, 0.5% (w/v) biocytin hydrochloride, 50 μ M Alexa Fluor 488 hydrazide; osmolality 290–295 mOsm; pH was adjusted to 7.3 with CsOH.

Visually guided whole-cell patch-clamp recordings from tdTomato-labeled Colgalt2-Cre neurons in V2M were performed using a Scientifica SliceScope Pro 3000 microscope equipped with a 40 \times , 0.8 NA objective and an infrared Dodt Gradient Contrast system. A COOLED pE-4000 light source (550 nm) was used to visualize fluorescence in Cre-expressing neurons. Before each recording, the apical dendrite was visually inspected to verify that it was not cut and could be seen to descend at a shallow angle into the slice. For neurons that were successfully filled with biocytin during the recording, we also confirmed that all dendrites, except a small number of basal and tuft dendrites extending directly toward the slice surface, were intact. Recordings were made with a MultiClamp 700B amplifier (Molecular Devices) in voltage-clamp configuration with a holding potential of -70 mV. Filtered signals (8 kHz low pass) were digitized at 20 kHz with a National Instruments data acquisition board (PCIe-6323). Acquisition and stimulus protocols were generated in Igor Pro (WaveMetrics) with the NeuroMatic software package (Rothman and Silver, 2018). Throughout each recording, series resistance compensation was set to the highest value possible without inducing oscillations in the cell (typically between 40 and 75%). Recordings with series resistance larger than 40 M Ω were discarded.

Patterned optogenetic stimulation. Optical stimulation was implemented using a digital micromirror device coupled to a 463 nm constant wave laser (Polygon 400, Mightex Systems). The stimulus consisted of a $1000 \times 500 \mu\text{m}$ grid divided into 24×12 spots of light ($41.7 \mu\text{m} \times 41.7 \mu\text{m}$ square) delivered through a $5\times/0.15$ NA objective (Olympus MPlanFLN). The grid was centered on the soma and aligned to the pia orthogonal to the apical dendrite. The laser output associated with each spot was measured (catalog #PM100D and #S121C, Thorlabs) and adjusted to obtain a measured power of $\sim 300 \mu\text{W}$ (173 mW/mm²). Optical stimuli were delivered for 1 ms at 10 Hz in a pseudo-random sequence designed to maximize the distance between consecutive spots and the time between stimulation of neighboring spots. Each recording trial consisted of a single repetition of all 288 stimuli followed by a full-field stimulus, in which all stimulation spots were illuminated simultaneously for 1 ms. Five to 20 trials were recorded, with 30 s pauses between trials, making the interval between consecutive stimulation of the same spot 60 s. An image of the recorded cell (filled with Alexa Fluor 488) relative to the stimulation grid was used during analysis to align the recorded sCRACM heatmap with the location of the pia or soma.

Immunohistochemistry and morphologic reconstructions. After recording, slices were fixed overnight at 4°C in a 4% paraformaldehyde solution and were subsequently kept in PBS. Slices were stained with DAPI (5 $\mu\text{g}/\text{ml}$) for 10 min, mounted on glass slides, and images were acquired with either a confocal microscope for high-resolution images (Leica SP5, objective $20\times/0.7$ NA or $10\times/0.4$ NA; pinhole size, 1 airy unit) or a slide scanner for visualizing injection sites (Olympus VS120, objective $4\times/0.16$ NA). Image processing was done with the FIJI software package. For the detailed morphologic analysis, a subset of neurons, selected based on the quality and completeness of staining, was reconstructed in full through the LMtrace service at <https://ariadne.ai/lmtrace>.

Comparison of axonal projection patterns across V2M subdivisions. We have extracted layer-wise axonal projection data for the 6 input areas [including all genotypes, anterior cingulate area (ACA), $n = 33$; anterior thalamic nuclei (ATN), $n = 11$; LP, $n = 10$; orbitofrontal cortex (ORB), n

$= 11$; retrosplenial area, granular part (RSPg), $n = 17$; primary visual area (VISp), $n = 60$] from the Allen Mouse Brain Connectivity database (<https://connectivity.brain-map.org/>). Projection energy followed the same layer-wise pattern across the three target areas for all input areas ($p > 0.05$, two-way ANOVA with Tukey's *post hoc* test) except for ACA [retrosplenial area, lateral agranular part (RSPagl) vs posteromedial visual area (VISpm), $p = 0.001$; anteromedial visual area (VISam) vs VISpm, $p = 0.016$]. When only wild-type data were considered, no statistical difference between target areas was detected ($p > 0.05$, two-way ANOVA with Tukey's *post hoc* test; $n = \text{ACA } 5, \text{ATN } 4, \text{LP } 2, \text{ORB } 2, \text{RSPg } 2, \text{VISp } 21$).

Data analysis. Analysis and data visualization were performed with custom scripts written in Igor Pro and MATLAB. Recordings were baseline in a 40 ms window before each stimulus and averaged across trials, and the peak and area (equivalent to the charge) of the evoked currents were measured in a 50 ms window after the stimulus. Currents with peaks greater than seven times the SD of the baseline were included in the analysis. Occasional cells showing low latency, direct photocurrent presumably resulting from retrograde infection were excluded from the analysis (ATN, 0/16; ORB, 0/18; ACA, 1/28; VISp, 0/14; V2M, 1/23; RSPg, 4/30; LP, 0/8 with 1:10 dilution and 11/17 with undiluted virus injection). Subsequently, recorded cells falling outside the borders of V2M were excluded. Heatmaps were normalized to the peak synaptic charge for each cell, aligned horizontally by soma location and vertically by either soma or pia location, and then averaged. Somas were localized to one quadrant of a single stimulation spot, resulting in a pixel dimension of $20.8 \times 20.8 \mu\text{m}$. Note, however, that the effective resolution is limited by light scattering and by the spread of voltage along stimulated axons. Previous studies have indicated that these factors limit the actual sCRACM resolution to $\sim 60 \mu\text{m}$ (Petreanu et al., 2009). Input maps for individual cells were convolved with the average ttL5 morphology obtained from 11 reconstructed V2M Colgalt2-Cre neurons. The apical tuft, oblique (including the apical trunk), and basal dendrites were manually labeled, and the total dendritic length was quantified in $10 \mu\text{m}$ bins along the apical dendrite axis using Neurolucida 360. The resulting dendrite profiles were aligned, averaged, and scaled to the soma–pia distance for each recorded cell. For testing Peters' rule, that is, to enable a direct comparison with the pia-aligned axon and sCRACM maps, morphologies were pia aligned before averaging. Axon and dendrite distributions were normalized to their respective peaks and multiplied, resulting in large values for predicted input at locations containing both axons and dendrites.

Experimental design and statistical analyses. Sufficient sample sizes were estimated based on similar published experiments performed in other brain regions (Petreanu et al., 2009; Young et al., 2021). Data are presented as mean \pm SEM unless specified otherwise. Statistical analyses were performed in MATLAB and were corrected for multiple comparisons using the Benjamini–Hochberg procedure where appropriate. Statistical tests used are specified and absolute p values are given.

Results

To ensure recording from a homogeneous neuronal population, we used the Colgalt2-Cre mouse line, which specifically labels subcortically projecting, ttL5 neurons (Groh et al., 2010; Kim et al., 2015). We focused our study on area V2M as higher order cortical regions are likely to receive a broader diversity of long-range inputs than primary sensory cortices. V2M is defined in the *Mouse Brain in Stereotaxic Coordinates* atlas (Franklin and Paxinos, 2007; Kirkcaldie, 2012), which can be used to guide viral injections. Furthermore, as this atlas is based on cytoarchitecture, V2M can be visually distinguished and selectively targeted in slice recordings as has been done previously (Galloni et al., 2020; Young et al., 2021). For whole-brain rabies tracing, on the other hand, we adopted the more recently developed CCFv3 (Wang et al., 2020a). This atlas allowed us to localize individual neurons within 3D volumes of brain tissue, which is not possible using

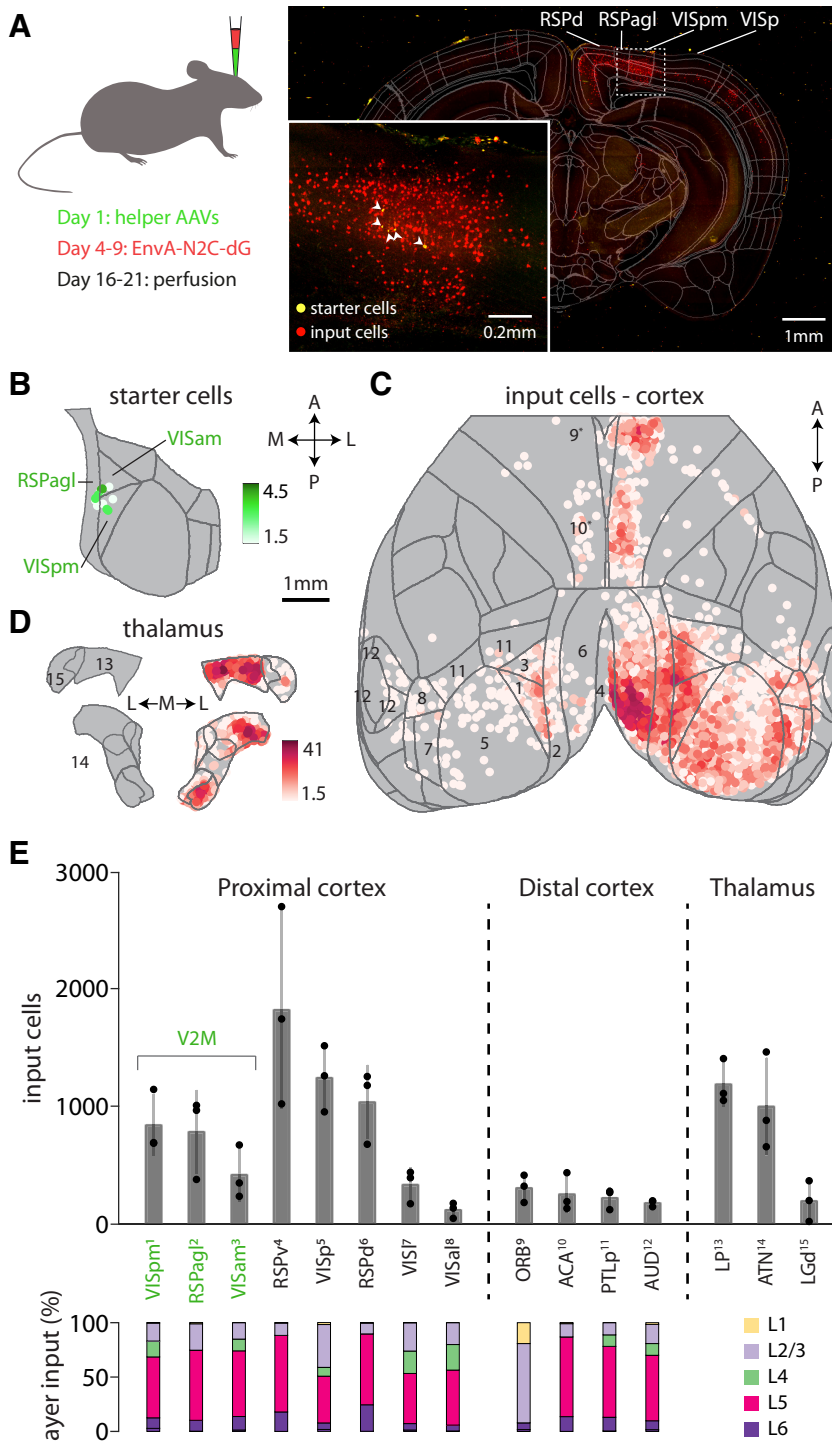


Figure 1. Whole-brain input map to V2M ttL5 neurons. **A**, Maximum intensity projection of a 200- μ m-thick coronal slab containing starter neurons, with Allen CCFv3 outlines overlaid. Inset, Starter area with higher magnification. **B**, Starter cell density map from an example experiment (same as in **A**). **C**, Cortical input cell density map projected onto the horizontal plane, same experiment as in **A**. **D**, Thalamic input cell density map projected onto two coronal planes, same experiment as in **A**. Density scales are in cells/0.01 mm²; arrows represent anterior, posterior, medial, and lateral directions. **E**, Input cell numbers for the most prominent input areas. Averages, SD, and individual experiments are shown. Bottom, Distribution of input cells across cortical layers. Named areas are marked with numbers in **C** and **D**; asterisks denote areas below the cortical surface. Area definitions and nomenclature according to the Allen CCFv3. Comprehensive cell counts for individual experiments can be found in Extended Data Figure 1-1.

the Franklin and Paxinos (2007) atlas. Within the CCFv3, the V2M region corresponds to areas VISpm, VISam, and RSPagl (Lyamzin and Benucci, 2019), all of which are known to be visually responsive (Garrett et al., 2014; Powell et al., 2020). Treating

V2M as a uniform region for the purposes of this study was also supported by the Allen Mouse Brain Connectivity database, which shows that axonal projections to VISpm, VISam, and RSPagl are not substantially different (see above, Material and Methods for details).

Brain-wide input map to V2M ttL5 pyramidal neurons

We used a monosynaptically restricted rabies virus approach (Wickersham et al., 2007; Reardon et al., 2016) to generate a pre-synaptic input map of V2M ttL5 neurons. Briefly, a mix of adeno-associated viruses carrying floxed N2c G-protein or TVA-receptor and EGFP genes were injected into V2M of *Colgalt2-Cre* mice under stereotaxic guidance. Four to 9 d later, mCherry-expressing EnvA-CVS-N2c- Δ G rabies virus was injected at the same location. After a further 12–13 d, brains were fixed and imaged using serial section 2-photon tomography (Fig. 1A). The resultant datasets were registered to the Allen CCFv3 atlas, and presynaptic cell bodies were detected and counted using an automated pipeline (see above, Materials and Methods for details).

Example images and cell density maps are shown in Figure 1. Starter cells were scattered across V2M (Fig. 1B), whereas presynaptic input neurons were detected in a broad range of cortical and subcortical areas (Fig. 1C,D). We have grouped the most prominent input areas into proximal cortex, distal cortex, and thalamus (Fig. 1E). Most input cells were found locally in V2M and in the proximal cortical areas VISp and the granular retrosplenial cortex (RSPg, consisting of the dorsal and ventral parts of the retrosplenial area, RSPd and RSPv). ORB and the ACA provided the most numerous distal cortical inputs. Interestingly, although most cortical input cells were detected in the granular and infragranular layers, especially layer 5, input from ORB was almost exclusively from layer 2/3 (Fig. 1E). Prominent thalamic inputs were also observed, originating mainly in the LP and ATN. Comprehensive cell counts for individual experiments can be found in Extended Data Figure 1-1.

To understand the subcellular organization of the diverse input pathways, we chose to examine seven prominent input areas. We grouped them in three categories based on their connectivity distance from the visual sensory periphery, VISp and V2M as FF input; RSPg, ACA, and ORB as cortical FB input; and LP and ATN for thalamic FB connections. We designate local (V2M) input as FF because ttL5 neurons are considered the outputs of the cortical column and show very limited local projections.

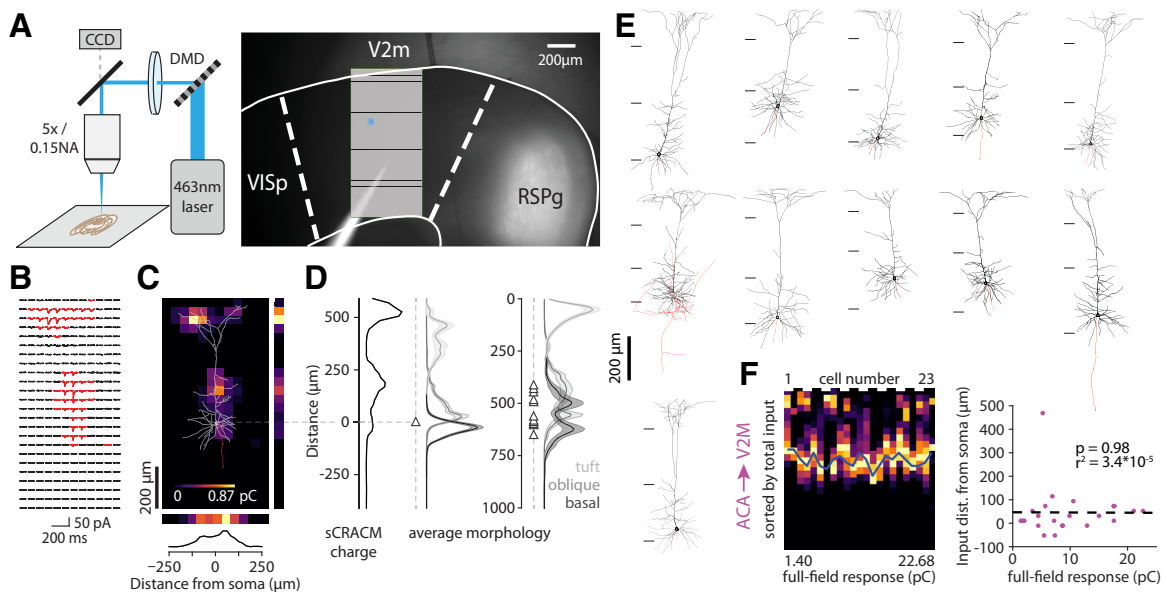


Figure 2. Using sCRACM to map subcellular connectivity. **A**, Experimental setup and micrograph showing a brain slice with Chronos expression in RSPg and recording pipette in V2M. The stimulation grid is overlaid, and an example spot is highlighted in blue. **B**, sCRACM recording of excitatory synaptic currents (red $> 7 \times$ baseline SD) from an example neuron. **C**, Charge heatmap corresponding to recording in **B** with the morphology of the recorded neuron overlaid. **D**, Left, Normalized vertical profile of the input map in **C**. Middle, Average soma-aligned morphologic profile used for dendritic domain deconvolution. Right, Averaged pia aligned morphologic profile. Triangles represent soma location. **E**, Morphologic reconstruction of 11 Colgalt2-cre neurons used for the average morphologic profile; dendrites, black; axons, red. Horizontal lines demarcate the border between L1–L2/3 and the top and bottom border of L5. **F**, Horizontal projections of ACA input to individual cells sorted by full-field stimulation response. Right, Location of the largest input peak versus full-field response. Dashed line is a linear fit.

Subcellular optogenetic input mapping reveals diverse targeting of dendritic domains by input areas

To determine the spatial distribution of synaptic inputs to ttL5 neurons in V2M, we performed sCRACM experiments from selected input areas identified by the rabies tracing. Following expression of the optogenetic activator Chronos in different input areas (see above, Materials and Methods for injection details), we made voltage-clamp recordings (at -70 mV) from tdTomato-labeled (Colgalt2-Cre) ttL5 neurons in V2M using acute brain slices. Optical stimulation with a 463 nm laser was spatially targeted using a digital micromirror device (Fig. 2A). Sodium and potassium channels were blocked using TTX ($1 \mu\text{M}$) and 4-AP ($100 \mu\text{M}$) to ensure that evoked currents were restricted to directly stimulated nerve terminals and to enhance presynaptic release, respectively. The stimulus consisted of 24×12 spots of light in a $1000 \times 500 \mu\text{m}$ grid aligned to the axis of the apical dendrite of the recorded neuron and covering the whole depth of cortex. We also quantified the total input from a given connection by recording synaptic currents evoked by full-field stimulation. To facilitate comparison between projections, we used the same laser intensity across all experiments.

Synaptic strength at each location was estimated by measuring the area of evoked synaptic currents (corresponding to charge; Fig. 2B) and creating normalized 2D maps of the spatial distribution of inputs (Fig. 2C). Individual maps were then aligned (either to the pia or soma) and averaged. To quantify the spatial location of inputs, we projected the average 2D maps in directions perpendicular (Fig. 2C) or parallel with the apical dendrite (Fig. 2D). Furthermore, we defined the spatial distribution of the three main dendritic compartments based on 11 morphologically reconstructed Colgalt2-Cre neurons (Fig. 2E). Basal dendrites were defined as those originating at the soma, oblique dendrites as those originating from the apical trunk before the main bifurcation

(including the apical trunk itself), and apical tuft dendrites as those originating after the bifurcation. As all three dendritic compartments have similar spine densities (Romand et al., 2011), the horizontal projection of the average morphology was used to separate the contribution of each dendritic domain to the total synaptic input (Fig. 2D).

One potential concern when recording distal synaptic currents from a somatic electrode is the effect of attenuation on detectability of currents. In neurons with weaker overall input, this might result in distal currents becoming too small to detect, thus biasing the input map toward the soma. We tested this by examining the correlation between the location of synaptic input and the total synaptic charge evoked by full-field stimulation (Fig. 2F). No correlation was found for any of the recorded areas ($p > 0.4$), suggesting that the passive distance-dependent attenuation introduced no detection bias for distal inputs.

Primary visual cortex

We first recorded optically evoked synaptic responses arising from VISp axons ($n = 9$ cells from six animals, average soma depth $507 \pm 22 \mu\text{m}$; Fig. 3A). The apical tuft received 42% of the input, with a peak input located $188 \mu\text{m}$ from the pia (Fig. 3A*b–d*). The remaining input was spread between the oblique compartment receiving 33% and basal dendrites receiving 26% of the total input (Table 2). More of the recorded neurons had the peak input in the apical compartment ($n = 5/9$), whereas four cells lacked apical input (Fig. 3A*e*). The horizontal input distribution showed a slight medial skew (toward RSPg), most prominent in the oblique ($63 \mu\text{m}$) and basal compartments ($42 \mu\text{m}$; Fig. 3A*f*, Table 2). The total synaptic charge measured via the somatic recording following full-field stimulation was 0.93 ± 0.11 pC (Fig. 3A*g*). VISp thus provides moderate direct input to ttL5 neurons in V2M, primarily targeting the proximal part of the apical tuft (0.39 pC) with smaller input arriving to the oblique (0.30 pC) and basal (0.24 pC) compartments.

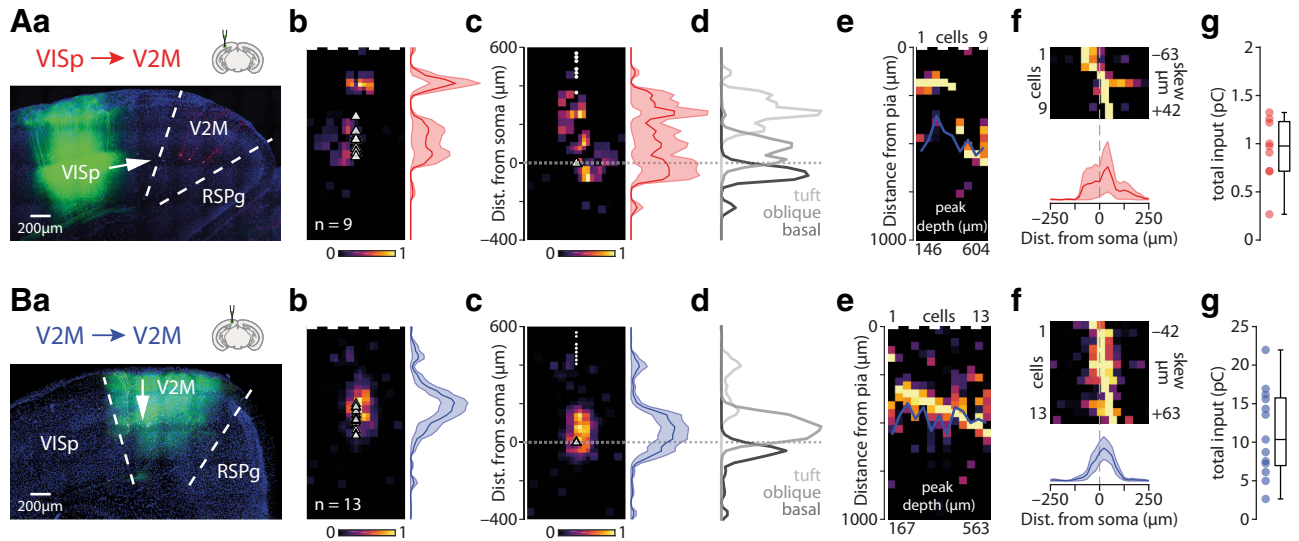


Figure 3. Subcellular connectivity maps of FF input areas. **Aa–g**, Confocal image of a representative brain slice (blue = DAPI) showing the injection site in VISp (green) and recorded neurons in V2M (red). **b**, Pia-aligned average sCRACM heatmap for VISp inputs. Triangles represent soma locations. The vertical profile indicates the normalized average and SEM of the input distributions across all recorded neurons. **c**, Same as in **b** but aligned on the soma location. Dots indicate pia locations. **d**, Normalized input magnitude deconvolved with the average morphology. Dotted line indicates soma location. **e**, Vertical projections of individual input maps sorted by the location of the peak input. **f**, Horizontal projections of individual input maps and their average. **g**, Box plot showing total input charge recorded during full-field stimulation. **B**, Same as in **A** but for Cre-off Chronos injections into V2M.

Table 2. Results of all sCRACM experiments

Input area	Parameter	Basal	Oblique	Tuft*		
VISp <i>N</i> = 6 <i>n</i> = 9	Peak location (μm)	−63	104	188	Total input (pC)	0.93
	Input proportion (%)	26%	33%	42%	Total input SEM	0.11
	Proportional input (pC)	0.24	0.30	0.39	Soma depth (μm)	507 ± 22
	Horizontal bias (μm) **	63	42	−21	Cells with peak in tuft	5/9
V2M <i>N</i> = 4 <i>n</i> = 13	Peak location (μm)	−42	83	167	Total input (pC)	11.24
	Input proportion (%)	24%	62%	14%	Total input SEM	1.56
	Proportional input (pC)	2.68	6.96	1.60	Soma depth (μm)	498 ± 15
	Horizontal bias (μm) **	21	21	−21	Cells with peak in tuft	1/13
RSPg <i>N</i> = 9 <i>n</i> = 20	Peak location (μm)	−42	42	125	Total input (pC)	3.40
	Input proportion (%)	30%	40%	30%	Total input SEM	0.51
	Proportional input (pC)	1.03	1.36	1.01	Soma depth (μm)	503 ± 15
	Horizontal bias (μm) **	21	21	0	Cells with peak in tuft	2/20
ACA <i>N</i> = 5 <i>n</i> = 23	Peak location (μm)	−42	42	83	Total input (pC)	9.46
	Input proportion (%)	30%	45%	25%	Total input SEM	1.32
	Proportional input (pC)	2.83	4.22	2.41	Soma depth (μm)	464 ± 9
	Horizontal bias (μm) **	0	0	−21	Cells with peak in tuft	1/23
ORB <i>N</i> = 3 <i>n</i> = 11	Peak location (μm)	−42	21	N/A	Total input (pC)	7.16
	Input proportion (%)	35%	57%	9%	Total input SEM	1.43
	Proportional input (pC)	2.47	4.05	0.64	Soma depth (μm)	521 ± 19
	Horizontal bias (μm) **	0	21	0	Cells with peak in tuft	0/11
ATN <i>N</i> = 3 <i>n</i> = 8	Peak location (μm)	−104	104	104	Total input (pC)	2.48
	Input proportion (%)	8%	17%	75%	Total input SEM	0.54
	Proportional input (pC)	0.20	0.42	1.86	Soma depth (μm)	435 ± 15
	Horizontal bias (μm) **	21	42	21	Cells with peak in tuft	6/8
LP <i>N</i> = 4 <i>n</i> = 10	Peak location (μm)	−42	21	63	Total input (pC)	0.97
	Input proportion (%)	10%	15%	75%	Total input SEM	0.16
	Proportional input (pC)	0.10	0.14	0.73	Soma depth (μm)	500 ± 23
	Horizontal bias (μm) **	−42	−21	−83	Cells with peak in tuft	9/10
	Total proportional input	27%	49%	24%	Sum total input (pC)	35.64

*Tuft measurements from pia, basal and oblique from soma; **negative distance means lateral, positive medial.

Local input from V2M

To estimate the distribution of local input we used a Cre-off viral strategy, limiting Chronos expression to non-Colgalt2-Cre neurons (*n* = 13 cells from four animals, average soma depth 498 ± 15 μm; Fig. 3B). When testing this strategy using the *Rbp4-Cre* line, which densely labels L5 pyramidal neurons, we found that

only a very small proportion (3%) of Cre-positive cells expressed Chronos. The peak input was located close to the soma, at 396 μm from the pia (Fig. 3Bb–d). The oblique compartment received the majority (62%) of this input, with the basal dendrites and apical tuft receiving 24% and 14%, respectively, of the total input (Table 2). For the majority of recorded neurons, the peak

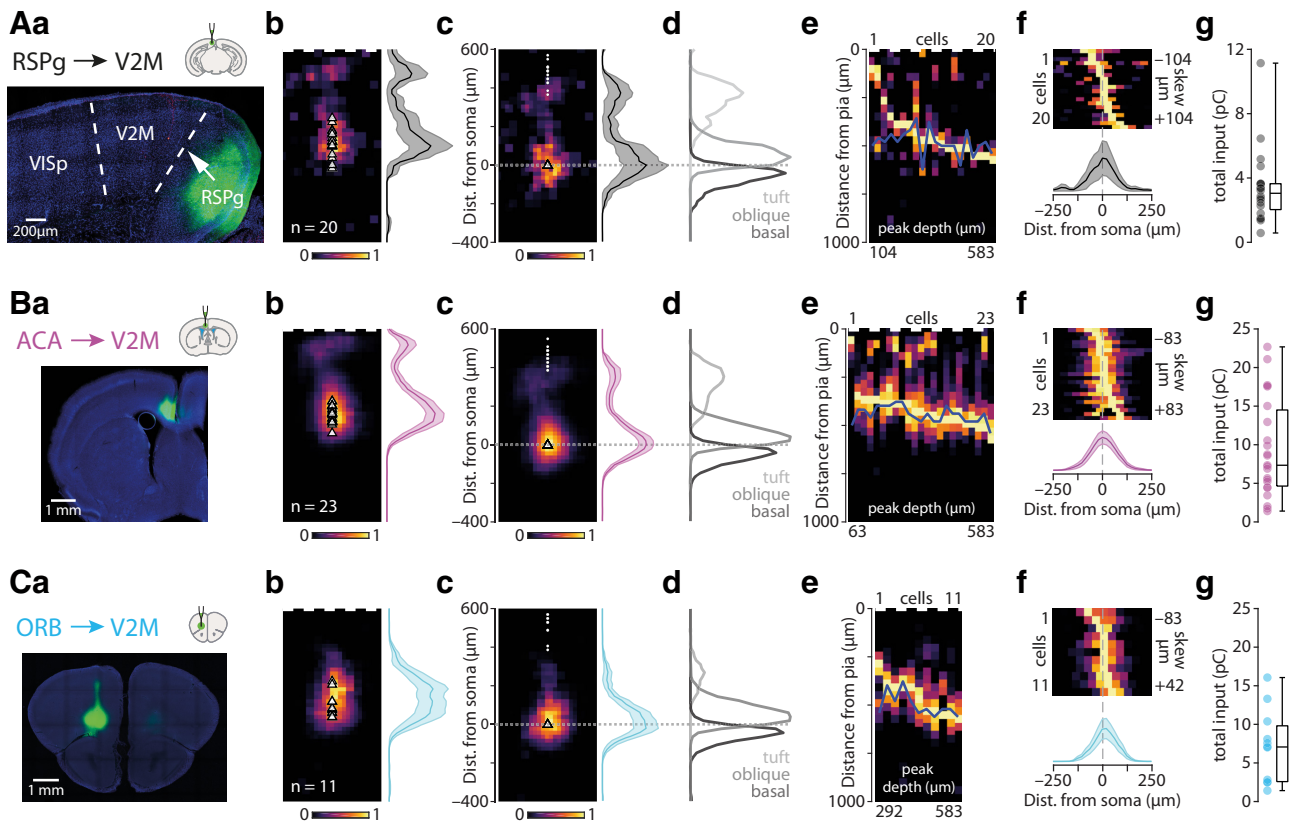


Figure 4. Subcellular connectivity maps of cortical FB areas. **Aa–f**, Confocal image of a representative brain slice (blue = DAPI) showing the injection site in RSPg (green). **b**, Pia-aligned average sCRACM heatmap for RSPg inputs. Triangles represent soma locations. The vertical profile indicates the normalized average and SEM of the input distributions across all recorded neurons. **c**, Same as in **b** but aligned on the soma location. Dots indicate pia locations. **d**, Normalized input magnitude deconvolved with the average morphology. Dotted line indicates soma location. **e**, Vertical projections of individual input maps sorted by the location of the peak input. **f**, Horizontal projections of individual input maps and their average. **g**, Box plot showing total input charge recorded during full-field stimulation. **B**, Same as in **A** but for Chronos injections into ACA. **C**, Same as in **A** but for Chronos injections into ORB.

input occurred perisomatically ($n = 12/13$; Fig. 3Be). The horizontal input distribution showed slight medial bias ($-21 \mu\text{m}$ for all peaks; Fig. 3Bf, Table 2). The total synaptic charge triggered by full-field stimulation was $11.24 \pm 1.56 \text{ pC}$ (Fig. 3Bg). Local neurons thus provide large direct input to tL5 neurons in V2M, primarily targeting the oblique (6.96 pC) compartment, with smaller input arriving to the basal (2.68 pC) and tuft (1.6 pC) compartments.

Granular retrosplenial area

Next, we recorded optically evoked synaptic responses arising from RSPg axons ($n = 20$ cells from nine animals, average soma depth $503 \pm 15 \mu\text{m}$; Fig. 4A). The overall input displayed a bimodal distribution peaking at 125 and $500 \mu\text{m}$ from the pia (Fig. 4Ab–d). The apical tuft received 30% of the input, with the oblique compartment receiving 40% and basal dendrites 30% of the total input (Table 2). For the majority of recorded neurons, the peak input targeted the perisomatic dendrites ($n = 18/20$; Fig. 4Ae). The horizontal input distribution showed slight medial bias (Fig. 4Af, Table 2). Total synaptic charge triggered by full-field stimulation was $3.40 \pm 0.51 \text{ pC}$ (Fig. 4Ag). RSPg thus provides a relatively moderate direct input to tL5 neurons in V2M, targeting the oblique (1.36 pC), basal (1.04 pC), and apical tuft (1.01 pC) compartments to similar extent.

Anterior cingulate area

Next, we recorded optically evoked synaptic responses arising from ACA axons ($n = 23$ cells from five animals, average soma

depth $464 \pm 9 \mu\text{m}$; Fig. 4B). The overall input was bimodal, peaking at $83 \mu\text{m}$ and $438 \mu\text{m}$ from the pia (Fig. 4Bb–d). The apical tuft received 25% of the input, with the oblique compartment receiving 45% and basal dendrites 30% of the total input (Table 2). The majority of recorded neurons had the peak input located perisomatically ($n = 22/23$; Fig. 4Be). The horizontal input distribution showed no mediolateral bias (Fig. 4Bf, Table 2). The total synaptic charge triggered by full-field stimulation was $9.46 \pm 1.32 \text{ pC}$ (Fig. 4Bg). ACA thus provides a large direct input to tL5 neurons in V2M, primarily targeting the oblique (4.22 pC) compartment with smaller input arriving to the basal (2.83 pC) and most distal part of the apical tuft (2.41 pC).

Orbitofrontal cortex

Optically evoked synaptic responses arising from ORB axons ($n = 11$ cells from three animals, average soma depth $521 \pm 19 \mu\text{m}$; Fig. 4C) showed a strong perisomatic bias, with a peak at $417 \mu\text{m}$ from the pia (Fig. 4Cb–d). The apical tuft received only 9% of all input, with the oblique compartment receiving 57% and basal dendrites 35% of the total input (Table 2). This distribution was also highly homogeneous across neurons, with almost all recorded neurons having their peak input in the perisomatic region ($n = 10/11$; Fig. 4Ce). The horizontal input distribution showed no lateral bias (Fig. 4Cf, Table 2). The total synaptic charge triggered by full-field stimulation was $7.16 \pm 1.43 \text{ pC}$ (Fig. 4Cg). ORB thus provides a large direct input to tL5 neurons in V2M, primarily targeting the oblique (4.05 pC) and

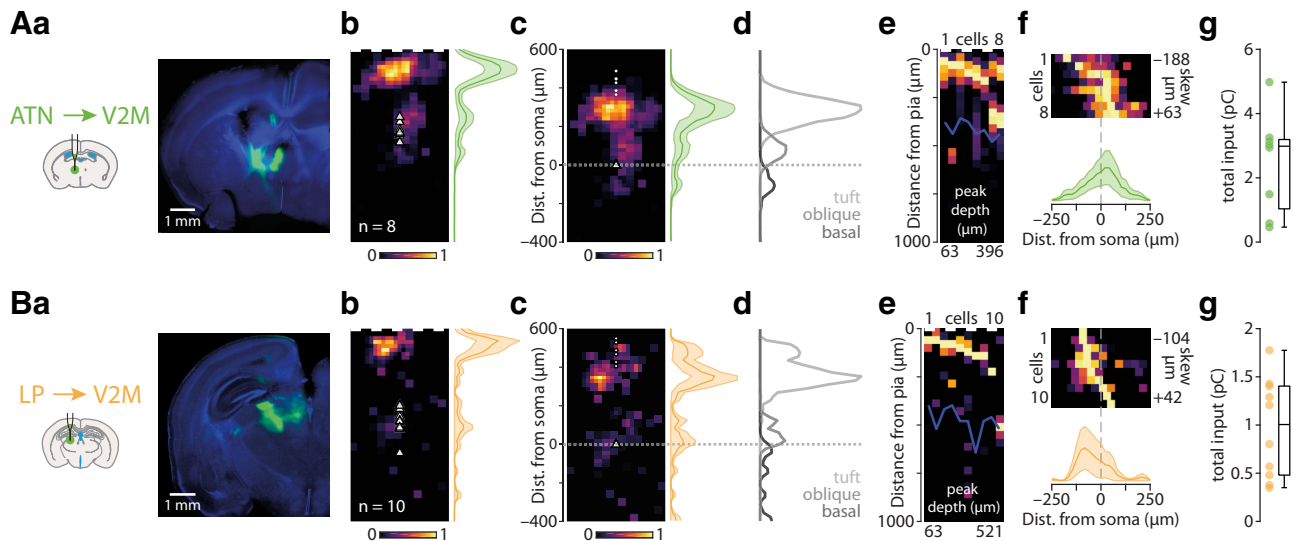


Figure 5. Subcellular connectivity maps of thalamic input areas. **Aa–f**, Confocal image of a representative brain slice (blue = DAPI) showing the injection site in ATN (green). **b**, Pia-aligned average sCRACM heatmap for ATN inputs. Triangles represent soma locations. The vertical profile indicates the normalized average and SEM of the input distributions across all recorded neurons. **c**, Same as in **b** but aligned on the soma location. Dots indicate pia locations. **d**, Normalized input magnitude deconvolved with the average morphology. Dotted line indicates soma location. **e**, Vertical projections of individual input maps sorted by the location of the peak input. **f**, Horizontal projections of individual input maps and their average. **g**, Box plot showing total input charge recorded during full-field stimulation. **B**, Same as in **A** but for Chronos injections in LP.

basal (2.47 pC) compartments, with slight input arriving to the proximal part of the apical tuft (0.63 pC).

Anterior thalamic nuclei

Next, we recorded optically evoked synaptic responses from thalamic axons, starting with the ATN ($n = 8$ cells from three animals, average soma depth $435 \pm 15 \mu\text{m}$; Fig. 5A). This input had peaks at both $104 \mu\text{m}$ and $333 \mu\text{m}$ from the pia (Fig. 5Ab–d). The apical tuft received the majority (75%) of the input, whereas the oblique compartment received 17% and basal dendrites a mere 8% of the total input (Table 2). The majority of recorded neurons had the peak input in the tuft compartment ($n = 6/8$), and although all cells had some tuft input, in 2/8 cells the input peak was located perisomatically (Fig. 5Ae). The horizontal input distribution showed a medial bias (Fig. 5Af, Table 2). The total synaptic charge triggered by full-field stimulation was 2.48 ± 0.54 pC (Fig. 5Ag). ATN thus provides a moderate direct input to ttL5 neurons in V2M, primarily targeting the more distal part of the apical tuft (1.86 pC), whereas the oblique (0.42 pC) and the basal (0.21 pC) compartments received less input.

Lateral posterior nucleus of the thalamus

Last, we recorded optically evoked synaptic responses arising from LP axons ($n = 10$ cells from four animals, average soma depth $500 \pm 23 \mu\text{m}$; Fig. 5B). Because of excessive retrograde labeling resulting in direct photocurrent in the recorded V2M cells, a 1:10 dilution of virus was used for these injections, and the absolute value of the evoked input is thus likely an underestimate. As with ATN axons, the LP input was strongly biased toward the most superficial part of the cortex and peaked at $63 \mu\text{m}$ from the pia (Fig. 5Bb–d). The apical tuft received the vast majority (75%) of the input, with the oblique compartment receiving 15% and basal dendrites 10% of the total input (Table 2). Most recorded neurons had the peak input in the tuft compartment ($n = 9/10$; Fig. 5Be). The horizontal input distribution showed lateral bias (Fig. 5Bf, Table 2). The total synaptic charge triggered by full-field stimulation was 0.97 ± 0.16 pC (Fig. 5Bg).

LP thus provides modest direct input to ttL5 neurons in V2M, primarily targeting the most distal part of the apical tuft (0.72 pC) compartment with smaller input arriving to the oblique (0.14 pC) and the basal (0.10 pC) compartments.

Comparison of anatomic and functional connectivity maps

Having determined the spatial distribution of synapses for the main input areas, we next sought to directly compare this to what would be predicted from axodendritic overlap (i.e., from Peters' rule). To determine axonal projection patterns from input areas to V2M, we have imaged the Chronos-EGFP-labeled axons in a subset of the brain slices used for the sCRACM experiments using confocal microscopy.

The spatial distribution of axons followed three basic patterns. Axons from VISp and ORB were densest in L2/3 and L5, whereas little projection was apparent in L1, reminiscent of the classical FF projection pattern (Fig. 6A). In contrast, axons from RSPg and ACA showed an FB-like pattern with dense labeling in the middle part of L1 followed by sparse labeling in L2 and diffuse axons in layers 3, 5 and 6 (Fig. 6B). The final group, which consists of the thalamic projections from LP and ATN, showed the classical FB pattern strongly innervating the external part of L1, with a secondary peak in L3, but little or no projections in layers 2, 5, and 6 (Fig. 6C).

To accurately estimate morphologic overlap between axons and dendrites, we multiplied the axonal projection maps with the average dendritic morphology, resulting in the predicted input distribution one would expect to see based on Peters' rule. When overlaying this with the pia-aligned vertical sCRACM maps, the alignments between functional synapses and the axodendritic maps were diverse (Fig. 7A). For some regions, like ORB perisomatic and LP tuft inputs, a clear correspondence could be seen between predicted and measured input distributions. A lesser degree of overlap can be seen in the VISp perisomatic or ACA tuft inputs. For other inputs, however, strong functional input could be detected where there is little overlap between dendrites and axons, such as at VISp tuft inputs. This

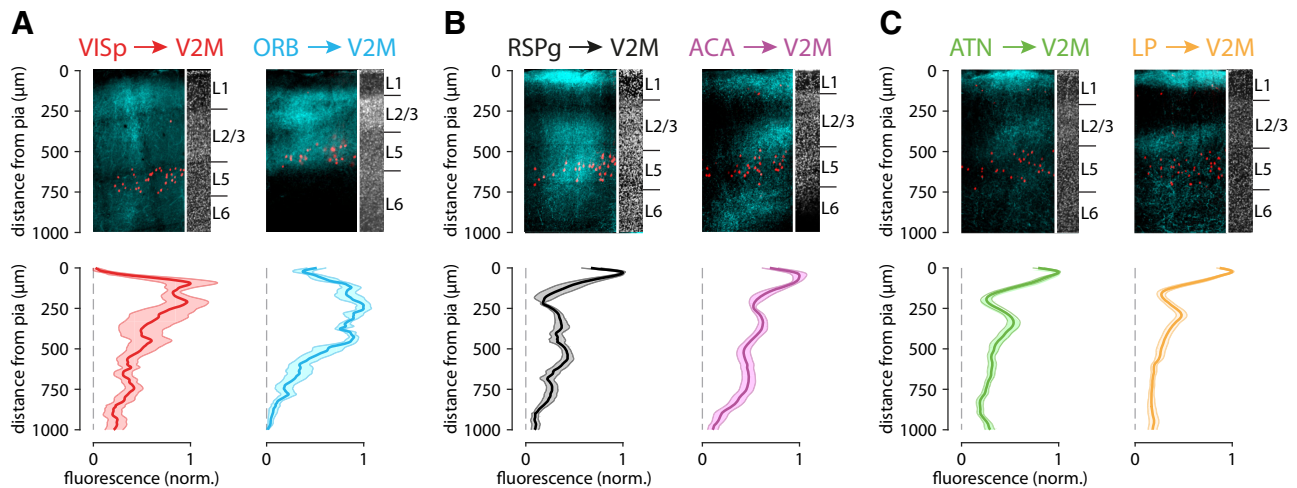


Figure 6. Axonal projection densities from different input areas. **A–C**, Top, Example confocal images from V2M showing axonal projections from six input areas (cyan) and Colgalt2-Cre cell bodies (red). The corresponding DAPI staining shows variation in laminar depth. Bottom, Average projection density profiles across the cortical depth averaged across 3–5 injections.

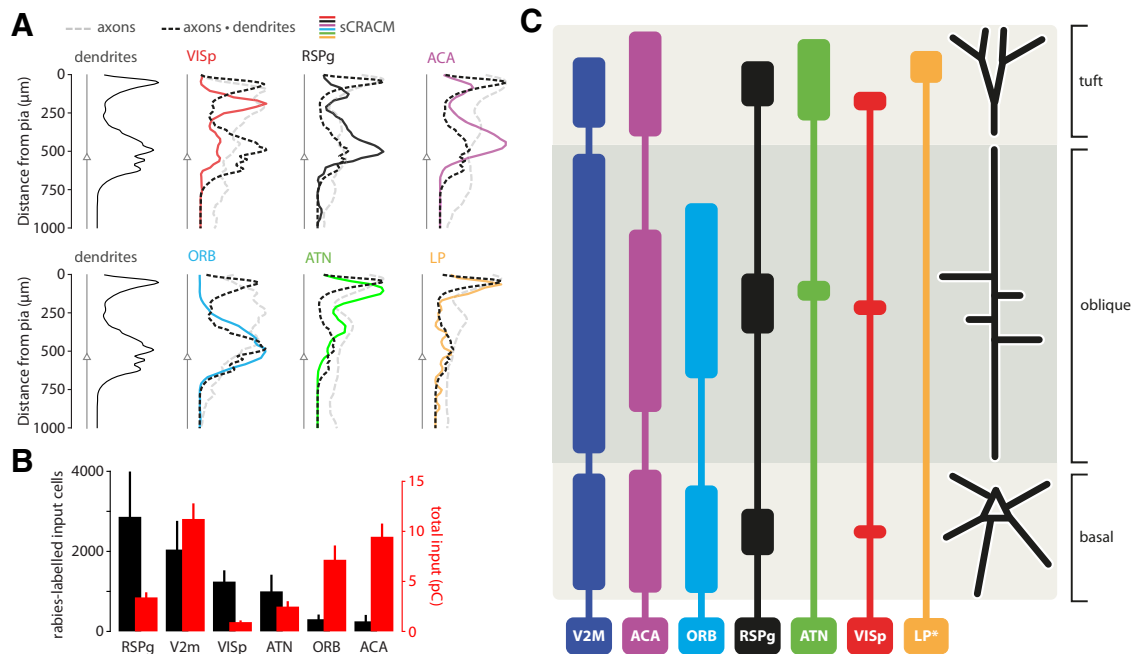


Figure 7. Comparison of different input maps. **A**, Axonal density distributions multiplied with dendritic morphology (dotted black lines) overlaid with pia-aligned synaptic input distributions (colored lines). Six input areas are shown. Triangles represent soma location in average morphology. **B**, Number of input cells across six areas established by rabies tracing (black) and total input charge recorded during full-field optogenetic stimulation (red). **C**, Schematic of excitatory synaptic input map to ttL5 pyramidal neurons. The height of bars represents input strength, whereas the center of each bar is aligned to the peak of the sCRACM map. The tuft input map was generated from pia-aligned maps, whereas oblique and basal maps are from soma-aligned maps. LP input magnitude (*) is likely underestimated because of the lower virus titer used.

stood in stark contrast to the ORB projection, for which the opposite was true, and apical regions of dense morphologic overlap of axons and dendrites resulted in no functional input.

Next, we examined the correspondence between the anatomic input connectivity obtained from rabies tracing and the functional connectivity measured by total synaptic input. The number of rabies-labeled input neurons showed a strong contribution from RSPg and V2M, and modest input cell numbers for the more distal cortical regions (e.g., ACA, ORB). The total synaptic input, however, shows no correlation with these numbers ($p = 0.8$, $r = -0.14$, Spearman's correlation; Fig. 7B), with modest synaptic input from RSPg and most input arriving from V2M, ACA, and ORB. Together, these results show clear specificity of dendritic

targeting by brain-wide connections, with only a loose adherence to Peters' rule for most inputs as well as large differences between anatomic and functional connectivity measured by rabies tracing and optogenetic stimulation, respectively.

Discussion

Using data from an array of techniques for long-range circuit dissection, we conducted a direct assessment of Peters' rule for brain-wide connections. Furthermore, we provide a comprehensive map of the dendritic targets of inputs to ttL5 neurons in area V2M in mice. Our recordings were targeted to V2M because cytoarchitectural definition of this region allows it to be

identified in brain slices. One limitation of this approach is that V2M can be subdivided into separate areas using retinotopic maps (Garrett et al., 2014; Zhuang et al., 2017) or anatomic projection patterns (Gilissen et al., 2021), which likely contribute to heterogeneity in connectivity. However, laminar distribution of axonal projections to VISpm, VISam, and RSPagl from the input areas examined in this study are highly similar in the Allen Mouse Brain Connectivity Atlas (see above, Materials and Methods) and we observed no clear differences in sCRACM responses attributable to cell locations, supporting our working assumption of uniform long-range connectivity across V2M.

The whole-brain input map generated via rabies tracing was qualitatively similar to previous results from the primary visual cortex (Kim et al., 2015). Axonal projections from the rabies-identified input regions broadly followed the expected pattern, with FB projections being biased toward L1 and FF toward the deeper layers (Rockland and Pandya, 1979; Harris et al., 2019; D'Souza et al., 2020). Accordingly, L1 was densely innervated by higher order areas like RSPg and ACA as well as the higher order thalamic nuclei (LP, ATN). Interestingly, ORB, although forming part of the frontal association cortex, displayed a projection pattern attributed to FF areas and had projection neurons mainly in L2/3, another feature of FF connectivity.

Compared with the axonal projection patterns, synaptic input maps across input areas showed a remarkable degree of heterogeneity. One technical caveat of measuring distal inputs through somatic voltage-clamp recordings is passive filtering along the dendrites. Although this is difficult to correct for in an unbiased way, we minimized filtering by using a Cs⁺-based internal solution. Additionally, we quantified the integral, which is less affected by filtering, instead of the peak of the evoked currents. Importantly, our data showed no correlation between response magnitude and response location, arguing against large errors caused by dendritic filtering.

To test Peters' rule, we compared anatomically predicted and functionally measured input maps. Several connections showed only weak correspondence between the two. For example, input from VISp, which is FF by definition and is assumed to primarily target perisomatic dendrites (Larkum, 2013), was instead biased toward the apical tuft. Conversely, although the axonal projection pattern from ORB was almost identical, synapses formed almost exclusively with basal and oblique dendrites, indicating highly specific dendritic domain targeting. Other recorded areas (RSPg, ACA, ATN) partially conformed to Peters' rule, yet still with significant differences between predicted and measured input distributions. The only area with strong adherence to Peter's rule was LP. Although it is possible that comparing individual axon, dendrite, and synaptic profiles on a single-cell basis would have given more accurate results, this was not possible as all three measures were not available for every neuron. However, the pattern of functional input from each input region was mostly consistent across cells. Morphologies of ttL5 neurons are likewise highly stereotypical, and averaging is thus warranted. Furthermore, axon projection patterns used for evaluating Peters' rule were measured from a subset of the same slices used for the sCRACM recordings, further supporting the direct comparison of predicted and functional input maps. The discrepancy resulting from averaging is thus likely to be low. Indeed, any smoothing resulting from averaging of morphologies, axonal projections, or sCRACM maps across the areas that make up V2M would only increase overlap and thus bias the results in favor of adhering to Peters' rule.

Comparing anatomic connectivity obtained by rabies tracing to functional connectivity obtained by full-field optogenetic stimulation revealed large and unexpected differences. There are, however, technical caveats that might bias this comparison. First, although every rabies-identified area showed synaptic input when testing with sCRACM, the quantitative accuracy of rabies tracing is highly debated (Rogers and Beier, 2021). Second, the magnitude of optogenetically evoked input depends on several technical parameters, such as infection efficiency and expression time. To facilitate comparison with rabies labeling, we maximized coverage for each input area by making several injections around the locations with highest rabies labeling density. Furthermore, there was no significant correlation between expression time and total input in any of the input areas ($n = 7$ areas, Benjamini–Hochberg correction with 0.1 false discovery rate) and area identity explained more variance than expression time ($r^2 = 0.44$ vs 0.11, $n = 95$ experiments). It is unlikely that these technical caveats alone could account for the remarkable discrepancy between anatomic and functional input magnitudes. There are several other possible explanations for this difference. First, axonal convergence may differ between input areas. For example, low convergence with one-to-one connectivity in inputs with strong rabies labeling could result in relatively weaker sCRACM input (VISp, RSPg). Meanwhile, strong synaptic currents relative to small rabies-labeled populations (ORB, ACA) may be explained by higher convergence. Such connections might be less discerning of their targets to convey more general contextual or state-specific information. Second, there may be a difference in the strength of individual synapses not reflected in rabies efficiency. A third contributing factor could be the recently reported activity dependence of rabies transmission (Beier et al., 2017). The apparent sparsity of some input areas (like ORB and ACA) could thus arise from having very low activity. Conversely, to result in extensive rabies labeling, VISp and RSPg should provide high-activity input.

It remains unclear what specific functions V2M serves. It has been linked to visual motion processing (Sun et al., 2009) and navigation and spatial processing as part of the dorsal stream (Glickfeld and Olsen, 2017; Powell et al., 2020). However, little is known about what exact processing on what specific information is done in this area. This is in contrast to primary sensory cortical areas, such as VISp and primary somatosensory cortex, where backpropagation activated calcium-spike (BAC) firing is a well-established dendritic mechanism linking apical tuft (assumed FF) and basal dendritic (assumed FB) inputs to support perception (Aru et al., 2020). In contrast, ttL5 neurons in V2M do not show BAC firing (Galloni et al., 2020), leaving local dendritic interactions to underlie their computational properties. Although the exact computations performed are yet to be unraveled, a recent study showed that pyramidal neurons can learn complex nonlinear functions by exploiting local dendritic mechanisms to optimize synaptic weights (Bicknell and Häusser, 2021). Knowledge of the dendritic distribution of input pathways thus provide key information for understanding which inputs are interacting locally during learning.

To explore the space of possible interactions between FF and FB inputs, we used a novel approach to allocate sCRACM input to specific dendritic compartments (Fig. 7C). Thalamic FB input, which targets the apical tuft, arrives from multiple higher order nuclei. Parts of ATN receive strong vestibular input (Rancz et al., 2015) and together with RSP are critical for the head-direction

system (Taube, 2007; Velez-Fort et al., 2018). Spatial and multi-sensory contextual information carried by LP inputs (Roth et al., 2016) thus likely interacts with FF visual input in the tuft compartment. Unlike thalamic input, cortical FB inputs target all three dendritic domains. Surprisingly, the strongest of these, ORB and ACA, could interact with the local FF input at the level of oblique and basal dendrites. Frontal cortices are generally involved in decision-making and motor control (Hamilton and Brigman, 2015), and ORB additionally encodes spatial goals (Feierstein et al., 2006). ACA, meanwhile, can regulate visual responses and sensory discrimination (Zhang et al., 2014), and contributes to predictive learning in V2M (Fiser et al., 2016). Their precise roles in the functioning of V2M, however, remains unknown. The strong input received by oblique dendrites is particularly important, as this compartment strongly affects L5 excitability (Schaefer et al., 2003) and can gate information flow from the apical dendrites (Jarsky et al., 2005). The particular targeting of ORB and ACA inputs to oblique dendrites might allow fine-level control of FF synapses at these dendrites while simultaneously enabling them to exert gating control over tuft-projecting input from both the thalamic nuclei and V2M.

Overall, our results show that although FF or FB classification can be based on axonal projections (albeit with exceptions, such as ORB), macroscopic projectomes do not predict cell-type-level input location. Consequently, there was no clear link between dendritic targeting and the organization of input areas in a cortical hierarchy. Furthermore, although rabies tracing is an effective tool to study general wiring diagrams, the proportion of input neurons thus estimated gives a poor estimate of functional input strength. Finally, the location and possible interactions between FF and the broad range of FB inputs, as well as their specific information content, suggests that tL5 neurons may be adopting a multitude of integrative strategies that are more complex than previously believed.

References

- Anastasiades PG, Collins DP, Carter AG (2021) Mediodorsal and ventromedial thalamus engage distinct L1 circuits in the prefrontal cortex. *Neuron* 109:314–30.e4.
- Aru J, Suzuki M, Larkum ME (2020) Cellular mechanisms of conscious processing. *Trends Cogn Sci* 24:814–825.
- Beier KT, Kim CK, Hoerbelt P, Hung LW, Heifets BD, DeLoach KE, Mosca TJ, Neuner S, Deisseroth K, Luo L, Malenka RC (2017) Rabies screen reveals GPe control of cocaine-triggered plasticity. *Nature* 549:345–350.
- Bicknell BA, Häusser M (2021) A synaptic learning rule for exploiting nonlinear dendritic computation. *Neuron* 109:4001–4017.e10.
- Briggman KL, Helmstaedter M, Denk W (2011) Wiring specificity in the direction-selectivity circuit of the retina. *Nature* 471:183–188.
- D'Souza RD, Wang Q, Ji W, Meier AM, Kennedy H, Knoblauch K, Burkhalter A (2020) Canonical and noncanonical features of the mouse visual cortical hierarchy. *bioRxiv*. doi: 10.1101/2020.03.30.016303.
- Feierstein CE, Quirk MC, Uchida N, Sosulski DL, Mainen ZF (2006) Representation of spatial goals in rat orbitofrontal cortex. *Neuron* 51:495–507.
- Felleman DJ, Van Essen DC (1991) Distributed hierarchical processing in the primate cerebral cortex. *Cereb Cortex* 1:1–47.
- Fino E, Yuste R (2011) Dense inhibitory connectivity in neocortex. *Neuron* 69:1188–1203.
- Fiser A, Mahringer D, Oyibo HK, Petersen AV, Leinweber M, Keller GB (2016) Experience-dependent spatial expectations in mouse visual cortex. *Nat Neurosci* 19:1658–1664.
- Franklin KJB, Paxinos G (2007) The mouse brain in stereotaxic coordinates. Amsterdam: Academic Press.
- Galloni AR, Laffere A, Rancz E (2020) Apical length governs computational diversity of layer 5 pyramidal neurons. *Elife* 9:e55761.
- Garrett ME, Nauhaus I, Marshel JH, Callaway EM (2014) Topography and areal organization of mouse visual cortex. *J Neurosci* 34:12587–12600.
- Gilissen SRJ, Farrow K, Bonin V, Arckens L (2021) Reconsidering the border between the visual and posterior parietal cortex of mice. *Cereb Cortex* 31:1675–1692.
- Glickfeld LL, Olsen SR (2017) Higher-order areas of the mouse visual cortex. *Annu Rev Vis Sci* 3:251–273.
- Groh A, Meyer HS, Schmidt EF, Heintz N, Sakmann B, Krieger P (2010) Cell-type specific properties of pyramidal neurons in neocortex underlying a layout that is modifiable depending on the cortical area. *Cereb Cortex* 20:826–836.
- Guerguiev J, Lillicrap TP, Richards BA (2017) Towards deep learning with segregated dendrites. *Elife* 6:e22901.
- Hamilton DA, Brigman JL (2015) Behavioral flexibility in rats and mice: contributions of distinct frontocortical regions. *Genes Brain Behav* 14:4–21.
- Han Y, Kechschull JM, Campbell RAA, Cowan D, Imhof F, Zador AM, Mrsic-Flogel TD (2018) The logic of single-cell projections from visual cortex. *Nature* 556:51–56.
- Harris JA, et al. (2019) Hierarchical organization of cortical and thalamic connectivity. *Nature* 575:195–202.
- Helmstaedter M, Briggman KL, Turaga SC, Jain V, Seung HS, Denk W (2013) Connectomic reconstruction of the inner plexiform layer in the mouse retina. *Nature* 500:168–174.
- Jarsky T, Roxin A, Kath WL, Spruston N (2005) Conditional dendritic spike propagation following distal synaptic activation of hippocampal CA1 pyramidal neurons. *Nat Neurosci* 8:1667–1676.
- Kasthuri N, et al. (2015) Saturated reconstruction of a volume of neocortex. *Cell* 162:648–661.
- Kim EJ, Juavinett AL, Kyubwa EM, Jacobs MW, Callaway EM (2015) Three types of cortical layer 5 neurons that differ in brain-wide connectivity and function. *Neuron* 88:1253–1267.
- Kim JS, Greene MJ, Zlateski A, Lee K, Richardson M, Turaga SC, Purcaro M, Balkam M, Robinson A, Behabadi BF, Campos M, Denk W, Seung HS (2014) Space-time wiring specificity supports direction selectivity in the retina. *Nature* 509:331–336.
- Kirkcaldie MTK (2012) Stereotaxic map of the mouse neocortex. In: *The mouse nervous system* (Watson C, Paxinos G, Puelles L eds), pp 52–111. San Diego, CA: Academic Press.
- Klein S, Staring M, Murphy K, Viergever MA, Pluim JP (2010) elastix: a toolbox for intensity-based medical image registration. *IEEE Trans Med Imaging* 29:196–205.
- Krishnaswamy A, Yamagata M, Duan X, Hong YK, Sanes JR (2015) Sidekick 2 directs formation of a retinal circuit that detects differential motion. *Nature* 524:466–470.
- Larkum M (2013) A cellular mechanism for cortical associations: an organizing principle for the cerebral cortex. *Trends Neurosci* 36:141–151.
- Lee WC, Bonin V, Reed M, Graham BJ, Hood G, Glattfelder K, Reid RC (2016) Anatomy and function of an excitatory network in the visual cortex. *Nature* 532:370–374.
- Little JP, Carter AG (2012) Subcellular synaptic connectivity of layer 2 pyramidal neurons in the medial prefrontal cortex. *J Neurosci* 32:12808–12819.
- Lyamzin D, Benucci A (2019) The mouse posterior parietal cortex: anatomy and functions. *Neurosci Res* 140:14–22.
- Niedworok CJ, Brown AP, Jorge Cardoso M, Osten P, Ourselin S, Modat M, Margrie TW (2016) aMAP is a validated pipeline for registration and segmentation of high-resolution mouse brain data. *Nat Commun* 7:11879.
- Osten P, Margrie TW (2013) Mapping brain circuitry with a light microscope. *Nat Methods* 10:515–523.
- Packer AM, McConnell DJ, Fino E, Yuste R (2013) Axo-dendritic overlap and laminar projection can explain interneuron connectivity to pyramidal cells. *Cereb Cortex* 23:2790–2802.
- Payeur A, Guerguiev J, Zenke F, Richards BA, Naud R (2021) Burst-dependent synaptic plasticity can coordinate learning in hierarchical circuits. *Nat Neurosci* 24:1010–1019.
- Petreanu L, Mao T, Sternson SM, Svoboda K (2009) The subcellular organization of neocortical excitatory connections. *Nature* 457:1142–1145.
- Powell A, Connelly WM, Vasalaukaite A, Nelson AJD, Vann SD, Aggleton JP, Sengpiel F, Ranson A (2020) Stable encoding of visual cues in the mouse retrosplenial cortex. *Cereb Cortex* 30:4424–4437.
- Ragan T, Kadiri LR, Venkataraju KU, Bahlmann K, Sutin J, Taranda J, Arganda-Carreras I, Kim Y, Seung HS, Osten P (2012) Serial two-photon

- tomography for automated *ex vivo* mouse brain imaging. *Nat Methods* 9:255–258.
- Rancz EA, Moya J, Drawitsch F, Brichta AM, Canals S, Margrie TW (2015) Widespread vestibular activation of the rodent cortex. *J Neurosci* 35:5926–5934.
- Reardon TR, Murray AJ, Turi GF, Wirblich C, Croce KR, Schnell MJ, Jessell TM, Losonczy A (2016) Rabies virus CVS-N2c(Δ G) strain enhances retrograde synaptic transfer and neuronal viability. *Neuron* 89:711–724.
- Rees CL, Moradi K, Ascoli GA (2017) Weighing the evidence in Peters' rule: does neuronal morphology predict connectivity? *Trends Neurosci* 40:63–71.
- Rieubland S, Roth A, Häusser M (2014) Structured connectivity in cerebellar inhibitory networks. *Neuron* 81:913–929.
- Rockland KS, Pandya DN (1979) Laminar origins and terminations of cortical connections of the occipital lobe in the rhesus monkey. *Brain Res* 179:3–20.
- Rogers A, Beier KT (2021) Can transsynaptic viral strategies be used to reveal functional aspects of neural circuitry? *J Neurosci Methods* 348:109005.
- Romand S, Wang Y, Toledo-Rodriguez M, Markram H (2011) Morphological development of thick-tufted layer v pyramidal cells in the rat somatosensory cortex. *Front Neuroanat* 5:5.
- Roth MM, Dahmen JC, Muir DR, Imhof F, Martini FJ, Hofer SB (2016) Thalamic nuclei convey diverse contextual information to layer 1 of visual cortex. *Nat Neurosci* 19:299–307.
- Rothman JS, Silver RA (2018) NeuroMatic: an integrated open-source software toolkit for acquisition, analysis and simulation of electrophysiological data. *Front Neuroinform* 12:14.
- Schaefer AT, Larkum ME, Sakmann B, Roth A (2003) Coincidence detection in pyramidal neurons is tuned by their dendritic branching pattern. *J Neurophysiol* 89:3143–3154.
- Sun B, Lv B, Dong Q, Wang S, Chai Z (2009) Watching moving images specifically promotes development of medial area of secondary visual cortex in rat. *Dev Neurobiol* 69:558–567.
- Taube JS (2007) The head direction signal: origins and sensory-motor integration. *Annu Rev Neurosci* 30:181–207.
- Tyson AL, Rousseau CV, Niedworok CJ, Keshavarzi S, Tsitoura C, Cossell L, Strom M, Margrie TW (2021) A deep learning algorithm for 3D cell detection in whole mouse brain image datasets. *PLoS Comput Biol* 17:e1009074.
- Velez-Fort M, Bracey EF, Keshavarzi S, Rousseau CV, Cossell L, Lenzi SC, Strom M, Margrie TW (2018) A circuit for integration of head- and visual-motion signals in layer 6 of mouse primary visual cortex. *Neuron* 98:179–91.e6.
- Vezoli J, Magrou L, Goebel R, Wang XJ, Knoblauch K, Vinck M, Kennedy H (2021) Cortical hierarchy, dual counterstream architecture and the importance of top-down generative networks. *Neuroimage* 225:117479.
- Wang Q, Ding SL, Li Y, Royall J, Feng D, Lesnar P, Graddis N, Naeemi M, Facer B, Ho A, Dolbeare T, Blanchard B, Dee N, Wakeman W, Hirokawa KE, Szafer A, Sunkin SM, Oh SW, Bernard A, Phillips JW (2020a) The Allen Mouse Brain Common Coordinate Framework: a 3D reference atlas. *Cell* 181:936–53.e20.
- Wang XJ, Pereira U, Rosa MG, Kennedy H (2020b) Brain connectomes come of age. *Curr Opin Neurobiol* 65:152–161.
- Wickersham IR, Lyon DC, Barnard RJ, Mori T, Finke S, Conzelmann KK, Young JA, Callaway EM (2007) Monosynaptic restriction of transsynaptic tracing from single, genetically targeted neurons. *Neuron* 53:639–647.
- Yamawaki N, Li X, Lambot L, Ren LY, Radulovic J, Shepherd GMG (2019) Long-range inhibitory intersection of a retrosplenial thalamocortical circuit by apical tuft-targeting CA1 neurons. *Nat Neurosci* 22:618–626.
- Young H, Belbut B, Baeta M, Petreanu L (2021) Laminar-specific cortico-cortical loops in mouse visual cortex. *Elife* 10:e59551.
- Zhang S, Xu M, Kamigaki T, Hoang Do JP, Chang WC, Jenvay S, Miyamichi K, Luo L, Dan Y (2014) Selective attention. Long-range and local circuits for top-down modulation of visual cortex processing. *Science* 345:660–665.
- Zhuang J, Ng L, Williams D, Valley M, Li Y, Garrett M, Waters J (2017) An extended retinotopic map of mouse cortex. *Elife* 6:e18372.